Quasar – CIV forest cross-correlation with SDSS DR12

Satya Gontcho A Gontcho,[1,3]* Jordi Miralda-Escudé,[1,2] Andreu Font-Ribera,[3]
Michael Blomqvist,[4] Nicolás G. Busca[5] and James Rich[6]

[1]*Institut de Ciències del Cosmos, Universitat de Barcelona/IEEC, Barcelona E-08028, Catalonia, Spain*
[2]*Institució Catalana de Recerca i Estudis Avançats, Barcelona E-08010, Catalonia, Spain*
[3]*Department of Physics & Astronomy, University College London, Gower Street, London, WC1E 6BT, UK*
[4]*Aix Marseille Université, CNRS, LAM, Laboratoire d'Astrophysique de Marseille, 13013 Marseille, France*
[5]*LPNHE, CNRS/IN2P3, Université Pierre et Marie Curie Paris 6, Université Denis Diderot Paris 7, 4 place Jussieu, 75252 Paris Cedex, France*
[6] *IRFU, CEA, Université Paris-Saclay, 91191 Gif-sur-Yvette, France*

ABSTRACT

We present a new determination of the large-scale clustering of the CIV forest (i.e. the absorption due to all CIV absorbers) using its cross-correlation with quasars in the Sloan Digital Sky Survey Data Release 12. We fit a linear bias model to the measured cross-correlation. We find that the transmission bias of the CIV forest, b_{Fc}, at a mean redshift of $z = 2.3$, obeys $(1 + \beta_c)b_{Fc} = -0.024 \pm 0.003$. Here, β_c is the linear redshift space distortion parameter of the CIV absorption, which can only be poorly determined at $\beta_c = 1.1 \pm 0.6$ from our data. The most accurately determined combination marginalized over β_c is $(1 + 0.44\,\beta_c)b_{Fc} = -0.0170 \pm 0.0014$. The transmission bias is related to the bias of CIV absorbers and their host haloes, $b_{\tau c}$, through the effective mean optical depth of the CIV forest, which we estimate at $\bar{\tau}_c(z) \simeq 0.01$ from previous studies of the CIV equivalent width distribution. We then find $1 < b_{\tau c} < 1.7$, with the large error arising from uncertainties in β_c and $\bar{\tau}_c$. This CIV bias is lower than the DLA bias $b_{\mathrm{DLA}} \simeq 2$ measured previously from the cross-correlation of DLAs and the Ly α forest, indicating that most CIV absorbers are hosted by haloes of lower mass than DLAs. More accurate determinations of $\bar{\tau}_c(z)$ and β_c are necessary to check this conclusion.

Key words: intergalactic medium – quasars: absorption lines.

1 INTRODUCTION

The doublet transition of triply ionized carbon (CIV) at 1548.204 and 1550.781 Å is one of the strongest and most common absorption lines probing intergalactic clouds that contain metals produced in stellar interiors. As a high-ionization species, CIV probes relatively low-density, unshielded gas, and is commonly present in Ly α absorption systems with column densities as low as $N_{\mathrm{HI}} \sim 10^{14} \, \mathrm{cm}^{-2}$ (e.g. D'Odorico et al. 2016), implying that heavy elements are present in a large fraction of the intergalactic medium. Studies of metal-absorption systems and their large-scale distribution, as probed by absorption spectra, can help us understand if intergalactic metals originated in numerous low-mass haloes where the primordial gas was first able to cool and form stars, or in more massive galaxies that ejected metal-loaded winds out to large distances and polluted vast volumes of intergalactic space. CIV systems are easily observed in the epoch when the global star formation rate in galaxies peaked, at a redshift $z \sim 2$–3 (e.g. Rauch, Haehnelt & Steinmetz

1997; Schaye et al. 2003; Hopkins & Beacom 2006; Boksenberg & Sargent 2015). Therefore, they can crucially contribute to our understanding of galaxy formation and evolution by probing gas in the process of cooling and accreting onto galaxies, as well as gas flowing out in winds.

Studying the large-scale clustering strength of CIV systems, in particular measuring their cross-correlation with other tracers of known auto-correlation, can help reveal the origin of these systems. On large scales, the clustering of any tracer can be described by linear theory, which depends on a linear bias factor that is monotonically related to the halo mass they reside in (e.g. Cole & Kaiser 1989; Tinker et al. 2010). Depending on the model assumed for the metal enrichment process, we expect different values for the clustering strength: if most CIV systems originated in stars forming in very low-mass haloes at all epochs, the gas should reflect the low bias factor of the smallest galaxies, whereas if the CIV gas was expelled to the intergalactic medium (IGM) in winds from massive star-forming galaxies, then their bias factor would be high, reflecting the highly biased nature of the most massive dark matter haloes . Detailed hydrodynamic simulations of galaxy formation can model

* E-mail: s.gontcho@ucl.ac.uk

the absorption line systems arising during the process of accretion of gas into galactic haloes and ejection by winds, making crucial predictions for testing our understanding of how galaxies form [see Bird et al. (2016) for a recent study].

Previous studies have estimated the clustering strength of individual CIV absorbers between redshift 1.5 and 4.5 (e.g. Lundgren et al. 2013; Vikas et al. 2013). In this paper, instead of using individually identified CIV absorption systems, we use spectral flux fluctuations blueward of the quasar CIV emission line as a continuous absorption field probing carbon-enriched gas in the Universe, similarly to the studies of the Ly α forest for atomic hydrogen . We refer to this continuous absorption field as the *CIV forest*. This approach has the advantage of including all the absorption systems, whether or not they are individually detected, and avoiding any dependence on the detection method. Using flux fluctuations directly has been done so far only for the Ly α forest, for which there was also a long debate about the nature of the absorption line systems as individual clouds or part of the intergalactic medium (e.g. Bahcall & Spitzer 1969; Lynds 1971; Sargent et al. 1980; Miralda-Escudé et al. 1996; Rauch 1998). The approach of measuring the Ly α forest clustering in terms of the power spectrum of the continuous absorption field, starting with Croft et al. (1998, 1999); McDonald et al. (2000); Croft et al. (2002); McDonald et al. (2006), has generally been very successful. In the linear regime, the overdensity of a tracer δ_t in real space relates to the overdensity in mass δ through the bias factor b as $\delta_t = b \cdot \delta$; it follows that the observed Ly α forest correlation function should be equal to the mass auto-correlation times the square of the mean bias factor of the Ly α transmission fluctuation, with the appropriate modifications of the well-known linear redshift space distortions (Kaiser 1987). Measurements of this Ly α auto-correlation have allowed the measurement of the value of the Ly α bias and redshift space distortion parameters (Slosar et al. 2011, 2013; Busca et al. 2013; Blomqvist et al. 2015; Delubac et al. 2015; Bautista et al. 2017). In addition to these measurements, the quasar bias has also been measured from its auto-correlation (Croom et al. 2005; Myers et al. 2007a,b; Shen et al. 2007; Coil et al. 2008; Ross et al. 2009; Shen et al. 2009; White et al. 2012; Eftekharzadeh et al. 2015; Laurent et al. 2017) and from its cross-correlation with the Ly α forest (Font-Ribera et al. 2013, 2014; du Mas des Bourboux et al. 2017), using the fact that the cross-correlation between two different probes is proportional to the product of bias factors of the two probes.

Similarly, here we measure the cross-correlation of quasars and the CIV forest at a mean redshift of $z = 2.3$ using the final data release of the Baryon Oscillation Spectroscopic Survey (BOSS) from the Sloan Digital Sky Survey 3rd edition (SDSS-III), inferring a CIV absorption fluctuation bias. Although the CIV forest is optically much thinner than the Ly α forest, and is therefore better described as individual absorbers for many applications, the alternative of directly measuring continuous fluctuations is still worth investigating.

The bias of the CIV forest large-scale transmission fluctuations, in the same way as for the Lyα forest, depends not only on the bias of the absorbing clouds or their host haloes, but also on the effective optical depth, $\bar{\tau}_c(z)$, quantifying the mean CIV transmission as a function of redshift, $\overline{F}_c(z) = \exp(-\bar{\tau}_c(z))$. We will see that the directly measurable fluctuation amplitude of CIV transmission fluctuations is proportional to $\bar{\tau}_c$, meaning that we need independent information on $\bar{\tau}_c(z)$ in order to translate the measured CIV forest bias to a bias of the absorbers, equal to that of their host haloes.

Measuring the bias factor of CIV forest transmission fluctuations is also useful to estimate the level of CIV contamination in cluster-

ing measurements of the Ly α forest, one of the main systematics studied in the recent Ly α analyses from the BOSS collaboration (Bautista et al. 2017; du Mas des Bourboux et al. 2017). An additional motivation to study the clustering of the CIV forest is to use it as a new tracer of the underlying mass density field that can probe the initial power spectrum, for example to measure the scale of Baryon Acoustic Oscillations Pieri (2014).

In parallel to the present work, Blomqvist et al. (2018) have completed a similar investigation including the larger data set of eBOSS. We compare and discuss the implications of the results in Section 7.3.

We start introducing the data samples used for this study in Section 2. In Section 3, we describe our procedure to obtain the transmission fluctuation in the CIV forest. Our method to infer the cross-correlation and fit a model is explained in Section 4. In Section 5, we present our measurement of the quasar-CIV forest cross-correlation and the inferred CIV bias factor. We discuss the interpretation of our results in terms of the bias factor of the CIV absorber host haloes in Section 7, and we conclude in Section 8. Throughout this work, we use a flat Λ cold dark matter cosmology with $h = 0.678$, $\Omega_m = 0.268$, $\Omega_b = 0.049$, $\sigma_8 = 0.815$, and $n_s = 0.968$, the best-fitting model to the CMB anisotropy power spectrum found in Ade et al. (2016).

2 DATA SETS

This paper uses the public twelfth Data Release (DR12; Alam et al. 2015) of the SDSS-III Collaboration (Fukugita et al. 1996; Gunn et al. 1998; York et al. 2000; Gunn et al. 2006; Eisenstein et al. 2011; Bolton et al. 2012), encompassing the entire 5 yr of observations of the Baryon Oscillation Spectroscopic Survey (BOSS; Dawson et al. 2013).

2.1 Quasar catalogue

The DR12 quasar catalogue,[1] described in Pâris et al. (2017), contains 297 301 quasars that were targeted for spectroscopy using the target selection procedure presented in Ross et al. (2012), which combines several algorithms to identify candidates described in Richards et al. (2009), Kirkpatrick et al. (2011), Yèche et al. (2010), and Bovy et al. (2011). We impose the redshift cut $1.4 \leq z_q \leq 4.2$, which reduces the catalogue to 231 312 quasars. We use the quasar redshifts obtained with the Principal Component Analysis method, as described in Pâris et al. (2012, 2014, 2017). The redshift distribution of the quasar catalogue is illustrated in Fig. 1 (left-hand panel).

2.2 CIV absorption spectra sample

We now define the set of spectra that we use for measuring the CIV absorption, which are different from the set of quasars described above. Starting again from the 297 301 quasars in the catalogue of Pâris et al. (2017), we first apply a cut to eliminate quasars with detected broad absorption lines (BALs). BALs appear in quasar spectra when jets pointing close to our direction launch matter at velocities of thousands of $km\,s^{-1}$, producing absorption features blueward of the Ly α and other emission lines that can be confused with intergalactic clouds between the quasar and us. The broadness
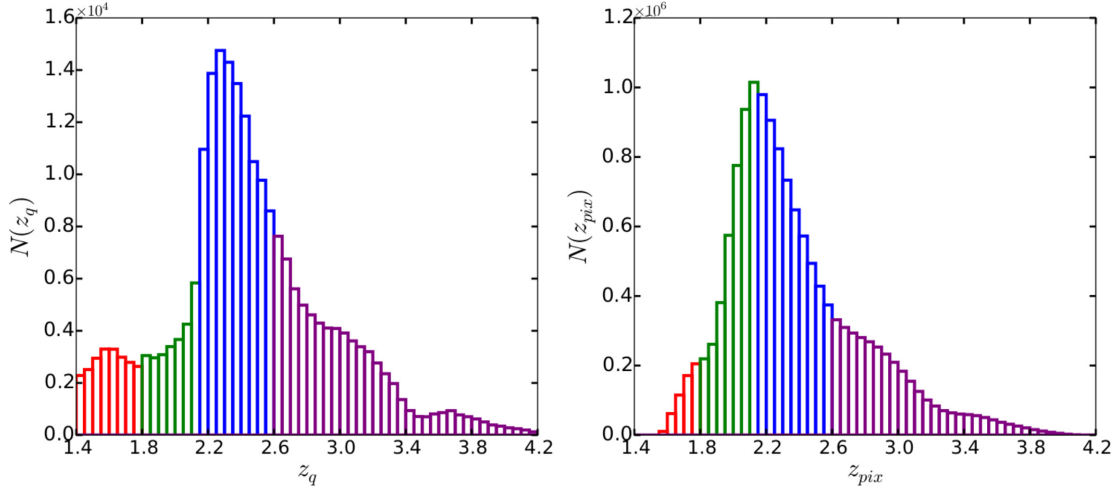

Figure 1. Left-hand panel presents the distribution of quasar redshift, and the right-hand panel presents the distribution of forest pixel redshifts (calculated with a mean CIV absorption wavelength at 1549.06 Å). Colours indicate the redshift intervals (described in Table 1) used throughout our analysis: $1.4 \leq z < 1.8$ (red), $1.8 \leq z < 2.15$ (green), $2.15 \leq z < 2.6$ (blue), and $2.6 \leq z \leq 4.2$ (purple).

of these lines, caused by the large velocity dispersion of the out-flowing gas, is used to identify BALs and classify quasars according to the 'balnicity index' (BI), introduced in Weymann et al. (1991). We eliminate all quasars that were flagged as BALs in the visual inspection. This leaves 265 889 quasars with a BI equal to zero in our sample.

We define the CIV forest to be the interval $1420 \,\text{Å} \leq \lambda_{RF} < 1520$ Å, where λ_{RF} is the quasar rest-frame wavelength. This avoids the region close to the quasar CIV emission line, which has a variable profile and is more sensitive to the presence of undetected BALs, and also the region that is affected by the SiIV quasar emission line and SiIV forest lines at lower wavelengths (see Fig. 2). We use the average wavelength of the unsaturated CIV doublet, $\lambda_c = 1549.06$ Å, to convert pixel wavelengths to redshifts in the CIV forest.

We apply a redshift cut for the quasar redshift of the spectra used to measure the CIV absorption, set to $1.8 \leq z_q \leq 4.2$, leaving 182 566 quasars. The lower limit is set by the requirement to have a margin on the blue side of the CIV forest to estimate the quasar continuum with the method that is described below in Section 3.1, and we do not use pixels below 3600 Å as the signal-to-noise ratio gets degraded for bluer wavelengths. As a result, only complete CIV forests are included in our work sample. The upper limit is set to the same maximum quasar redshift of 4.2 used above, beyond which the BOSS surface density of quasars is not sufficient to be useful for this study.

We remove pixels in which the variance of the co-added sky-subtracted sky fibres is significantly higher than in neighbouring pixels. The DR12 sky mask provides a list of these observed-frame wavelengths.[2] To apply the mask, we remove any pixels with an observed wavelength, λ, in the range

$$\text{abs} \left[10^4 \times \log_{10}(\lambda/\lambda_{mask}) \right] \leq m, \tag{1}$$

for any λ_{mask} in the list, where m is the margin. We use a margin of 1.5. Note that pixels in the BOSS co-added spectra have a wavelength width of $\Delta \log_{10}\lambda = 10^{-4}$.

The final cut we make on the spectra used for measuring the CIV absorption is related to our method to determine a quasar continuum.

We define for this purpose two spectral zones surrounding the CIV forest that avoid the SiIII, SiIV, and CIII emission lines: the first zone, referred to as Λ_1, is $1280 \,\text{Å} \leq \lambda_{RF} \leq 1380$ Å, and the second zone Λ_2 is $1575 \,\text{Å} \leq \lambda_{RF} \leq 1860$ Å, where $\lambda_{RF} = \lambda/(1 + z_q)$ is the quasar rest-frame wavelength. A spectrum is retained in our sample if the following condition for the signal-to-noise is satisfied in these two regions:

$$\frac{1}{n_{pc}} \sum_i (f_{si}/\sigma_{si}) \geq 2, \tag{2}$$

where the sum is done over all pixels in regions Λ_1 and Λ_2, f_{si} and σ_{si} are the observed flux and noise in a pixel i of spectrum s, and n_{pc} is the total number of pixels in the sum, in both regions Λ_1 and Λ_2. After the spectra that do not reach this minimum average signal-to-noise are eliminated, our sample is reduced to 140 813 lines of sight, with the redshift distribution of pixels in the CIV forest region ($1420 \,\text{Å} \leq \lambda_{RF} < 1520$ Å) shown in Fig. 1 (right-hand panel).

3 FROM FLUX IN THE BOSS SPECTRA TO THE CIV TRANSMISSION FLUCTUATION δ_c

3.1 Continuum fitting

To obtain the fraction of absorbed flux due to the presence of CIV systems in each spectrum we need a *continuum* model for each quasar, which is the quasar flux that would be observed in the absence of any intervening absorption. We use a weighted average of the sample of CIV absorption spectra defined in Section 2.2 for our continuum model, with weights that are proportional to the square of the signal-to-noise. We first derive normalizing coefficients of the flux for each spectrum s in our sample, in our two normalizing intervals

$$c_{s1} = \sum_{i \in \Lambda_1} (w_{si} f_{si}) \Big/ \sum_{i \in \Lambda_1} (w_{si}), \tag{3}$$

$$c_{s2} = \sum_{i \in \Lambda_2} (w_{si} f_{si}) \Big/ \sum_{i \in \Lambda_2} (w_{si}), \tag{4}$$

where the sum is over all pixels i of a spectrum s that belong to the Λ_1 region for c_{s1}, and the Λ_2 region for c_{s2}. The observed flux at every

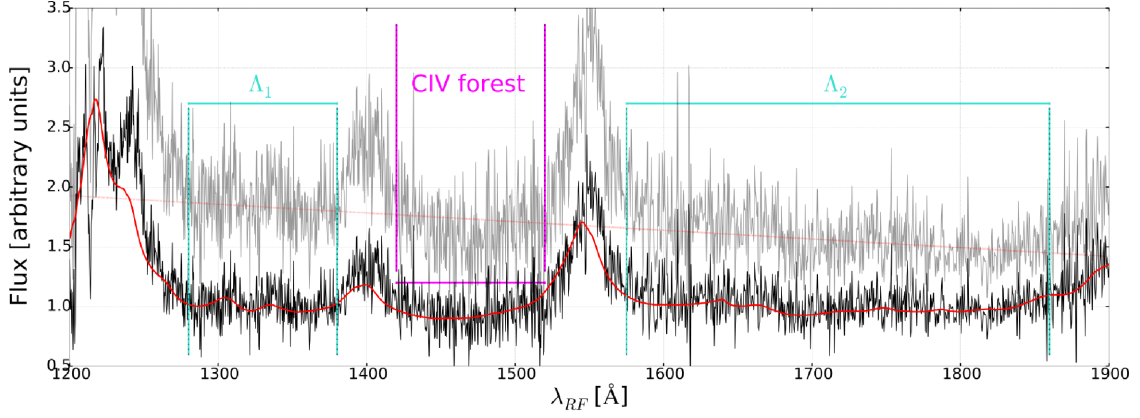[2]https://github.com/igmhub/picca/blob/master/etc/dr12-sky-mask.txt

Figure 2. Illustration of our procedure to estimate the mean quasar continuum in the CIV forest region, for the BOSS quasar spectrum at $RA = 1.490°$, $DEC = 13.582°$, $z = 2.896$, reference PLATE=6177, MJD=56268, FIBER=55, and THINGID=232251732. The grey spectrum is the observed spectrum f_s. The red dashed line is the linear regression to the mean flux in regions Λ_1 and Λ_2 (shown by vertical dotted turquoise lines), and the black spectrum $\hat{f}_{si}$ is the normalized flux after dividing by the linear regression. The red solid line is the mean quasar continuum introduced in equation (8). The magenta vertical lines mark the CIV forest region we use.

pixel is f_{si} and the weight is set to the inverse variance, $w_{si} = 1/\sigma_{si}^2$ (where σ_{si} is the noise in every pixel as estimated by the SDSS pipeline). The linear regression to the flux in each spectrum from these mean values is

$$L_{si} = c_{s1} + \frac{c_{s2} - c_{s1}}{\lambda_2 - \lambda_1}(\lambda_i - \lambda_1), \tag{5}$$

where λ_i is the observed wavelength of pixel i, and λ_1 and λ_2 are the mean observed wavelengths of regions Λ_1 and Λ_2 [with the pixels weighted the same way as c_{s1} and c_{s2} in equations (3) and (4)]. The normalized flux in each spectrum, after dividing by the mean value and removing the spectral tilt between regions Λ_1 and Λ_2, is

$$\hat{f}_{si} = \frac{f_{si}}{L_{si}}, \tag{6}$$

and the weight assigned to this normalized flux is set proportional to the square of the signal to noise

$$\hat{w}_{si} = L_{si}^2 w_{si}. \tag{7}$$

Finally, we compute the weighted mean quasar continuum at a given restframe wavelength, C_i, as

$$C_i = \sum_s (\hat{w}_{si} \cdot \hat{f}_{si}) \Big/ \sum_s \hat{w}_{si}, \tag{8}$$

where the sum is now over all quasar spectra. Fig. 2 illustrates this normalizing procedure for an example spectrum.

Note that by using normalization regions outside of the CIV forest, as highlighted on Fig. 2, we do not systematically remove any fluctuations and we avoid having to correct for continuum distortions as in other BOSS analyses [e.g. discussion on distortion matrix in du Mas des Bourboux et al. (2017) and Bautista et al. (2017)].

3.2 Flux transmission fraction in the CIV Forest

The flux transmission fraction can now simply be defined as $\hat{f}_{si}/C_i$ in every pixel. However, the optimal weights to be used for every spectrum to measure the CIV cross-correlations may vary from those in equation (7), depending on how strong the intrinsic sampling variance is compared to the observational noise, and this can change the mean value of the transmission fraction. We therefore define the flux transmission fluctuation including a global correcting

factor m_i [similar to $\bar{F}(z)$ used for analysis of Ly α forest correlations in Bautista et al. (2017)],

$$\delta_{c,si} = \frac{\hat{f}_{si}}{C_i m_i} - 1. \tag{9}$$

Note that while C_i is a function of restframe wavelength, m_i is a function of observed wavelength.

The correction m_i is to ensure that the mean fluctuation is equal to zero when averaged over all the spectra in any given sample, and depends on new weights W_{si} that we use for measuring correlations of $\delta_{c,si}$

$$m_i = \sum_s \left(W_{si}\frac{\hat{f}_{si}}{C_i}\right) \Big/ \sum_s (W_{si}). \tag{10}$$

In this paper, we shall use weights taking into account an intrinsic sampling noise at every pixel of σ_{int}, arising from the shot noise of the CIV absorbers themselves, plus any other metal-lines or intrinsic variations in the quasar spectra. This sampling variance implies that spectra at very high signal-to-noise should not be weighted in proportion to the inverse variance arising from the observational error, because the intrinsic variance dominates the contributed error to any correlation measurement. The optimal weight to use is

$$W_{si} = \left[(C_i^2 \times \hat{w}_{si})^{-1} + \sigma_{\text{int}}^2\right]^{-1}. \tag{11}$$

The correction factor m_i ensures that

$$\sum_s W_{si}\delta_{c,si} = 0, \tag{12}$$

which guarantees that measured correlations of $\delta_{c,si}$ go to zero in the limit of large separations.

In the limit when the CIV forest absorption is mainly caused by saturated systems that absorb most of the flux in one pixel, the optimal intrinsic dispersion is $\sigma_{\text{int}} \sim (1 - \bar{F}_c)^{1/2}$, where $\bar{F}_c$ is the mean transmission fraction. In practice the optimal value of σ_{int} is a little smaller because lines are not fully saturated. We shall estimate below from the observations of Cooksey et al. (2013) a value $1 - \bar{F}_c \simeq 0.01$, and we will generally use a characteristic intrinsic dispersion $\sigma_{\text{int}} = 0.08$, which we have found to be near optimal by trying several values of this parameter.

Table 1. Redshift intervals used in this analysis, with their mean redshift and the proportion of the whole sample of CIV spectra included in each one. The redshift interval names are: $\mathbb{F}$ for *full*, $\text{v}\mathbb{L}$ for *very low*, $\mathbb{L}$ for *low*, $\mathbb{M}$ for *medium*, and $\mathbb{H}$ for *high*.

Name	*z*-range	$\langle z \rangle$	Proportion
$\mathbb{F}$	1.4–4.2	2.2981	100 %
$\text{v}\mathbb{L}$	1.4–1.8	1.7225	4 %
$\mathbb{L}$	1.8–2.15	2.0325	20 %
$\mathbb{M}$	2.15–2.6	2.327	63%
$\mathbb{H}$	2.6–4.2	2.8519	13%

4 QUASARS-CIV FOREST CROSS-CORRELATION

This section describes how we measure the cross-correlation of the CIV transmission fluctuation δ_c with quasars, and how we fit it to a linear analytic model.

4.1 Sub-samples

The DR12 sample of CIV spectra described in 2.2 is divided into 2370 sub-samples, corresponding to the 2370 observational plates of the final DR12 data release of SDSS-III BOSS. Using directly the observational plates has the advantage that the sub-samples are of similar sizes and shapes. The distribution of these plates in the sky in equatorial coordinates is shown in Fig. 3. These sub-samples will be used to estimate the cross-correlation and its covariance matrix via the bootstrap method, combined with a smoothing mechanism to reduce sampling noise.

Apart from the sky sub-sampling, the CIV spectra are also divided into four redshift intervals in which we separately measure the cross-correlation. Table 1 specifies the redshift range, the redshift average, and the proportion of pixels in the CIV forest in each of the four intervals.

4.2 Estimator for the CIV transmission – quasar cross-correlation

Our method to estimate cross-correlations closely follows that of Font-Ribera et al. (2012), where the cross-correlation of Damped Ly α (DLAs) with the Ly α forest was measured. The comoving separation between any CIV spectral pixel and a quasar is expressed in terms of its perpendicular and parallel components, $r_\perp = D_A(z)(1+z)\,\Delta\theta$ and $r_\parallel = c/H(z)\,\Delta z$, which we calculate from the angular and redshift separations $\Delta\theta$ and Δz, and the angular diametre distance $D_A(z)$ and Hubble constant $H(z)$ at redshift z. We measure the cross-correlation in bins of 4 h^{-1} Mpc, both in the parallel and perpendicular separation, out to maximum values of 64 h^{-1} Mpc. There are therefore a total of $16 \times 32 = 512$ bins, since the separation $r_\perp$ is positive and has 16 bins, and $r_\parallel$ may have positive or negative sign and has 32 bins. The sign of $r_\parallel$ is defined to be positive when the CIV pixel is at higher redshift than the quasar.

We designate as $\xi_{\mathcal{P},A}$ the measured cross-correlation of quasars and the CIV transmission fluctuation δ_c in a plate (or sub-sample) $\mathcal{P}$, and a bin A in $(r_\parallel, r_\perp)$. The set of pairs of a quasar and a spectral pixel i contributing to $\xi_{\mathcal{P},A}$ satisfy two conditions: (a) the pixel i belongs to a spectrum s located in plate $\mathcal{P}$, and (b) the separation between the quasar and pixel i is within the bin A. The cross-correlation is

computed as

$$\xi_{\mathcal{P},A} = \sum_{s \in \mathcal{P}, i \in A} \left(W_{si}\,\delta_{c,si} \right) \Big/ W_{\mathcal{P},A},$$

$$\text{where} \qquad W_{\mathcal{P},A} = \sum_{s \in \mathcal{P}, i \in A} W_{si}. \qquad (13)$$

The sums here are extended over all the spectral pixels belonging to plate $\mathcal{P}$, and over all the quasars that are at a separation from pixel i that is within bin A. Note that often a bin i in $\mathcal{P}$ may not appear in the sum if there is no quasar within bin A, but it may also appear repeatedly if more than one quasar is at a separation within bin A. The quasars may be in a plate different from $\mathcal{P}$ because the angular separation from the CIV spectrum may take it outside the plate. In practice, this can be calculated by looping over all pairs of spectra and quasars, and adding the terms in equation (13) to the corresponding bins A for each pixel i. The final cross-correlation is obtained as

$$\xi_A = \sum_{\mathcal{P}} W_{\mathcal{P},A}\,\xi_{\mathcal{P},A} / W_A,$$

$$\text{where} \qquad W_A = \sum_{\mathcal{P}} W_{\mathcal{P},A}. \qquad (14)$$

4.3 The covariance matrix

The covariance matrix of the values of the cross-correlation in any two bins A and B is

$$C_{AB} = \langle \xi_A \xi_B \rangle - \langle \xi_A \rangle \langle \xi_B \rangle. \qquad (15)$$

We can obtain this covariance matrix from the values of the cross-correlation obtained in many independent sub-samples. If we neglect the small correlations among neighbouring sub-samples due to the correlated large-scale structure, the covariance can be expressed as

$$C_{AB} = \frac{1}{W_A W_B} \sum_{\mathcal{P}} W_{\mathcal{P},A} W_{\mathcal{P},B} \left[\xi_{\mathcal{P},A} \xi_{\mathcal{P},B} - \xi_A \xi_B \right]. \qquad (16)$$

However, for this covariance matrix to be reliably obtained in this way, its total number of elements needs to be considerably smaller than the number of sub-samples, $N_p = 2370$. The covariance matrix is actually extremely large (it is a symmetric 512×512 matrix), so it cannot be computed in this way directly. Instead, we follow the procedure used and described in Delubac et al. (2015), Bautista et al. (2017), and du Mas des Bourboux et al. (2017), Pérez-Ràfols et al. (2018). We start by defining the normalized covariance matrix, referred to as the correlation matrix:

$$\rho_{AB} = \frac{C_{AB}}{\sqrt{C_{AA} C_{BB}}}. \qquad (17)$$

To a good approximation, we find that ρ_{AB} is a function only of $\Delta r_\perp = |r_{\perp,A} - r_{\perp,B}|$ and $\Delta r_\parallel = |r_{\parallel,A} - r_{\parallel,B}|$. We average this correlation matrix over all bin pairs having the same $\Delta r_\perp$ and $\Delta r_\parallel$. This averaged correlation matrix has only $16 \times 32 = 512$ elements, which are sufficiently well determined from our 2370 sub-samples. Finally, we re-compute a smoothed covariance matrix C_{AB} from equation (17), using the averaged correlation matrix and the original values for the diagonal elements C_{AA} and C_{BB}.

Values of the correlation matrix are shown in Fig. 4 when averaged over our full redshift interval, which shows that the most important correlation coefficients are for $\Delta r_\perp = 0$. The correlation is primarily due to pairs of pixel-quasar pairs sharing the same quasar
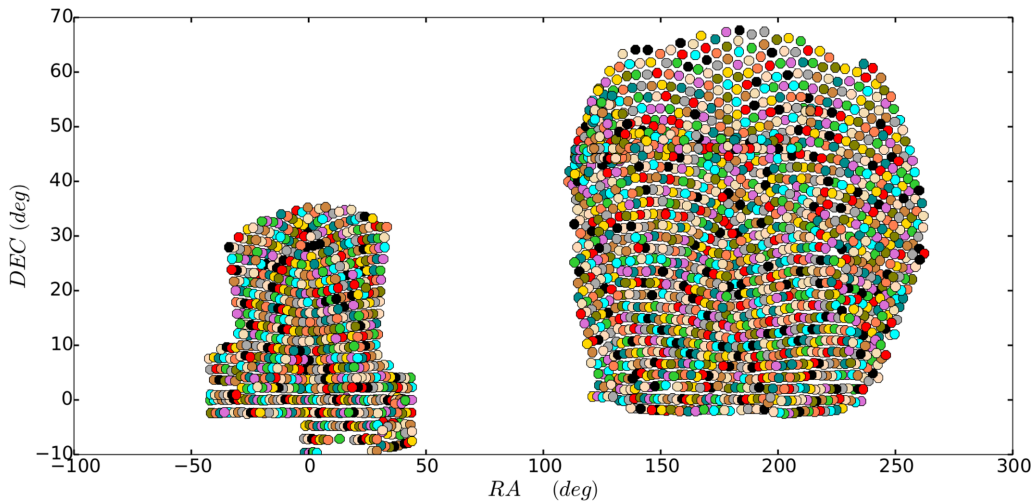
Figure 3. DR12 footprint, in J2000 equatorial coordinates, of the 2370 plates, equal to our sub-samples, shown in different colours as a visualization aid. The left (right) area is the South (North) Galactic Cap. The fixed dot size representing each plate is arbitrary and indicates only the centre of the plate, not its actual size.
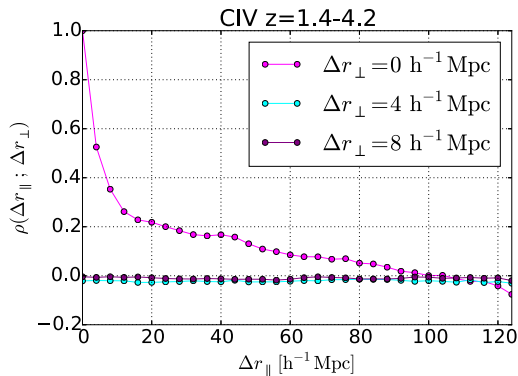

Figure 4. The averaged correlation $\rho_{AB} = C_{AB}/\sqrt{C_{AA}C_{BB}}$ as a function of $\Delta r_{\parallel} = |r_{\parallel,A} - r_{\parallel,B}|$, shown for perpendicular separations $\Delta r_{\perp} = |r_{\perp,A} - r_{\perp,B}| = 0$ (magenta), $\Delta r_{\perp} = 4\,h^{-1}$ Mpc (cyan) and $\Delta r_{\perp} = 8\,h^{-1}$ Mpc (purple).

and the same spectrum, which appear at $\Delta r_{\perp} = 0$ [see Section 4.3 and Appendix A.2 of du Mas des Bourboux et al. (2017)].

4.4 Fitting the CIV bias

In the limit of large scales, we can model the cross-correlation of any two tracers of the large-scale density field using linear theory (Kaiser 1987). Even though the scale at which we clearly detect the cross-correlation of quasars and CIV absorption reaches out to only $\sim 10\,h^{-1}$ Mpc, where linear theory may not be very accurate even at the high-redshift we make our measurements, it still provides a good model when combined with a velocity dispersion that can account for non-linear peculiar velocities in addition to quasar redshift errors and the intrinsic profile of the CIV doublet line. Following the same formalism as in Font-Ribera et al. (2012), the linear cross-correlation between a transmission fluctuation δ_c and a set of objects like our quasar sample can be expressed in terms of its Fourier transform or cross-power spectrum,

$$P_{Qc}(\mathbf{k}, z) = b_{Fc}(z)\,[1 + \beta_c(z)\,\mu_k^2]$$
$$\cdot b_q(z)[1 + \beta_q(z)\,\mu_k^2]\,P_L(k, z), \qquad (18)$$

where b_{Fc} is the bias factor of the CIV transmission fluctuation, b_q is the quasar bias factor, and β_c and β_q are the redshift space distortion parameters for CIV and for quasars. The bias b_{Fc} is not the usual bias factor describing the large-scale distribution of a population of objects, but is similar to the Ly α forest bias factor that relates a transmission fluctuation to a linear mass density fluctuation on large scales (see Slosar et al. 2011; Font-Ribera & Miralda-Escudé 2012): it has a negative value because a mass overdensity results in a reduced transmission, and a very small absolute value that reflects the small average absorption of the CIV forest and the corresponding small fluctuation in the transmission. This will be clarified in Section 7, where the relation of b_{Fc} to the bias factor of the population of CIV absorbers will be discussed. The linear matter power spectrum is $P_L(k, z)$; as expressed in equation (18), the amplitude of each Fourier mode in a biased tracer field is enhanced by the redshift distortion factor $b_{Fc}(z)[1 + \beta_c(z)\,\mu_k^2]$ of the CIV absorption, and by the corresponding factor for the quasars, where μ_k is the cosine of the angle between $\vec{k}$ and the line of sight.

We complement this linear theory formula by multiplying P_{Qc} by a Gaussian in the parallel direction, with a dispersion $\sigma_{\parallel}^{-1}$ (where the cross-correlation is convolved with a Gaussian with dispersion $\sigma_{\parallel}$), and adding a shift Δv in the parallel direction to account for a possible systematic in the quasar redshift error that displaces the centre of the cross-correlation. The dispersion can account for non-linearities, peculiar velocity dispersions of the quasar and CIV clouds, quasar redshift errors, and the mean profile of the CIV doublet line. The convolution of all these functions is approximated as a Gaussian in our analysis. We ignore any effect of the continuum fitting, which is less important than for the Ly α forest (e.g. Bautista et al. 2017) because of the low mean absorption by metal lines and the fact that we do not use the flux in the CIV forest interval itself to determine the continuum.

We make use of the fitting tool Baofit[3] developed in the context of the BOSS collaboration (Kirkby et al. 2013; Blomqvist et al. 2015) to compute parametrized fits with equation (18) of correlations of any tracer populations.

---

[3] http://darkmatter.ps.uci.edu/wiki/DeepZot/Baofit

The signal to noise of our detection of the CIV-quasar cross-correlation is not high enough to simultaneously fit a large number of parameters. We fix the quasar bias and redshift distortion factors to values determined from other observations, and we vary four free parameters: the CIV transmission bias and redshift distortion parameters, which are assumed constant in redshift, and the mean shift and dispersion in the parallel direction. The mean shift is assumed constant with redshift as a velocity, while the dispersion is assumed constant in comoving spatial units.

The fit is done over a range in $r = (r_\parallel^2 + r_\perp^2)^{1/2}$ from 5 to 60 h^{-1} Mpc. Any bins centred at values of r outside this range are excluded from the fit. This is done to exclude the central values which are more strongly affected by non-linear effects and the CIV doublet line shape, and to have a more isotropic distribution of bins.

We assume that there is no redshift evolution for the CIV bias and that the quasar bias follows the power-law evolution:

$$b_q(z) = b_q(z_{\rm ref}) \left(\frac{1+z}{1+z_{\rm ref}} \right)^{\gamma_q}, \qquad (19)$$

with $b_q(z_{\rm ref}) = 3.91$ at $z_{\rm ref} = 2.39$, and $\gamma_q = 1.7133$. This power law was fitted to the recent measurements of quasar clustering presented in Laurent et al. (2016).

5 RESULTS

In this section, the results of the redshift space cross-correlation of the CIV absorption with quasars are presented. After obtaining fits to our fiducial model, we check the consistency of our estimated errors from the smoothed covariance matrix and the bootstrap method.

5.1 The quasar – CIV forest cross-correlation

Fig. 5 shows this cross-correlation for the full redshift interval ($\mathbb{F}$ sample). The cross-correlation is in general negative because the overdensity near the quasar induces a negative fluctuation of the transmission fraction δ_c (or a positive fluctuation of the absorbed fraction by CIV systems). There is a clear detection at small separations, and a strong radial elongation at $r < 8\,h^{-1}$ Mpc which is expected from non-linear peculiar velocities, redshift errors, and the CIV doublet absorption line. The linear redshift space distortion causing a tangential elongation is not clearly detected.

We can better visualize the form of the cross-correlation in the radial direction in Fig. 6 which shows the values measured in the bins $0.0 < r_\perp < 4.0\,h^{-1}$ Mpc, as a function of $r_\parallel$, for the different redshift samples. The black squares with error bars are the same in every plot and they show results for the $\mathbb{F}$ sample, to be compared with the same measurements at every redshift interval. The four redshift intervals are shown in the four separate plots as coloured lines, and the shaded areas indicate $1 - \sigma$ error bars. There is no clear evidence for any variation of the cross-correlation with redshift. Only at the lowest redshift interval (the $\mathrm{v}\mathbb{L}$ sample) there is an indication of a stronger cross-correlation amplitude, but the difference is not highly significant. Note that the more precise determination of ξ is for the $\mathbb{M}$ redshift interval, because it contains more than half of all the quasar-pixel pairs, and has therefore strongly correlated results with the $\mathbb{F}$ sample. The lowest number of pairs occurs for the $\mathrm{v}\mathbb{L}$ sample, which has the largest errors.

Finally, in Fig. 7 the cross-correlation is shown for the $\mathbb{F}$ sample in three bins of perpendicular separation, from 4 to 16 h^{-1} Mpc. The amplitude of the cross-correlation variation declines with $r_\perp$ as expected.
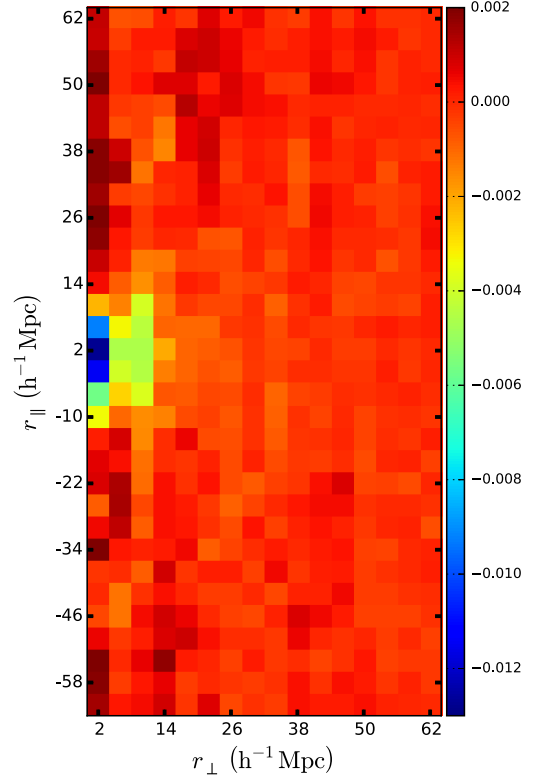

Figure 5. Contour plot of the quasar-CIV cross-correlation for the $\mathbb{F}$ sample covering the full redshift range, as a function of transverse separation $r_\perp$ and parallel separation $r_\parallel$.

5.2 Fits to the CIV transmission bias parameter

We obtain several fits of the quasar-CIV cross-correlation to the model described in Section 4.4, in the redshift intervals defined in Table 1. The parameters we fit are the combination $(1 + \beta_c)b_{Fc}$, where b_{Fc} is the CIV bias, the CIV redshift distortion parameter β_c, the velocity shift Δ_v, and the dispersion in quasar redshift $\sigma_\parallel$. We start with a fit with all 4-parameters allowed to vary for the full redshift interval $\mathbb{F}$, with the result shown in the first row of Table 2. We find that β_c has a large error because of the high degeneracy with $\sigma_\parallel$, which is broken only by measurements at large r with a low signal-to-noise ratio.

We therefore present fits with β_c fixed to three different values, to see the variation of the other parameters when β_c changes. As discussed below, the redshift distortion parameter is related to the bias factor of the CIV absorbers, $b_{\tau c}$, by $\beta_c = f(\Omega)/b_{\tau c}$, where $f(\Omega)$ is logarithmic derivative of the growth factor that appears in linear theory Kaiser (1987). A value $\beta_c = f(\Omega) \simeq 1$ corresponds to the case where CIV absorbers have the same large-scale fluctuation amplitude as the mass density perturbations, while $\beta_c = 0.5$ is expected if CIV absorbers are biased in the same way as DLAs Pérez-Ràfols et al. (2018). The values of χ^2 indicate that all these fits are consistent with the data within the uncertainties. The shift parameter Δ_v remains practically constant, while $\sigma_\parallel$ increases as β_c is increased. This correlation of the fit parameters occurs because increasing β_c makes the contours of the cross-correlation more tangentially elongated, while increasing $\sigma_\parallel$ makes them more radially elongated.

Then we fix β_c, Δ_v, and $\sigma_\parallel$ to the values measured in the first fit, and we do a 1-parameter fit in each of the four redshift sub-samples.
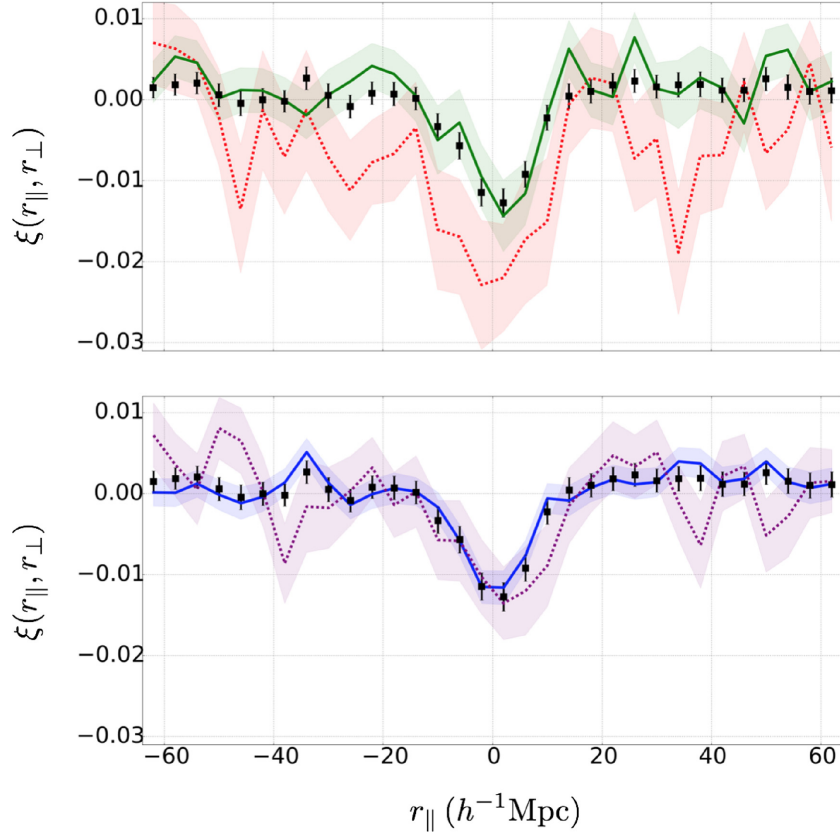
Figure 6. Comparison of the quasar-CIV cross-correlation at the $0 < r_\perp < 4\,h^{-1}$ Mpc bins, as a function of $r_\parallel$, for different redshift samples (previously described in Table 1). Respectively between: the $\mathbb{F}$ sample (black points with errorbars, for full redshift interval), on the upper panel the v$\mathbb{L}$ sample in red (dotted coloured line with shaded area indicating errors, for the lowest redshift interval) and the $\mathbb{L}$ sample in green solid line (green shaded area for the errors) and on the lower panel the $\mathbb{M}$ sample in blue solid line (blue shaded area for the errors) and the $\mathbb{H}$ sample in purple (dotted coloured line with shaded area indicating errors, for the highest redshift interval).
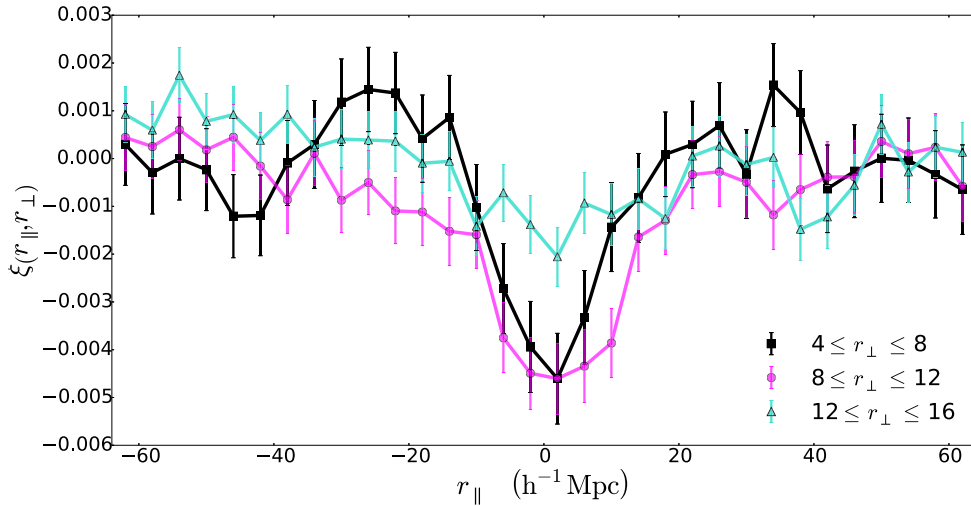

Figure 7. Cross-correlation for the $\mathbb{F}$ sample for the indicated perpendicular separation $r_\perp$ bins (in units of comoving h^{-1} Mpc), as a function of line-of-sight separation $r_\parallel$.

These results are presented in the bottom four rows of Table 2. There is no evidence for any redshift variation of the bias factor b_{Fc}. This transmission bias factor stays constant within ~ 20 per cent over our entire redshift range.

5.3 Bootstrap evaluation of the error

To verify the robustness of the smoothing of the covariance matrix described in Section 4.3, we estimate the error on the combination $(1 + \beta_c)b_{Fc}$ by bootstrap analysis with the 2370 plate measurements

Table 2. Results of the fit parameters $(1 + \beta_c)b_{Fc}$, β_c, Δ_v, and $\sigma_{\shortparallel}$. The first row is for all 4 parameters left free. In the next three rows, we fix the parameter β_c to the values indicated and leave free the other three parameters. The bottom four rows are 1-parameter fits to each of the four redshift sub-samples, varying only b_{Fc} and keeping the other 3 parameters to the same values as in the first row. If the other parameters were allowed to vary, the marginalized error bars of the bias would be larger, but the quoted errors indicate the uncertainty on the bias evolution if we assume the other parameters do not vary significantly.

	$(1 + \beta_c)b_{Fc}$	β_c	Δ_v (km s^{-1})	$\sigma_{\shortparallel}$ (h^{-1} Mpc)	χ^2	dof
$\mathbb{F}$	-0.024 ± 0.003	1.09 ± 0.56	-119.7 ± 52.4	4.75 ± 0.83	351.092	$356 - 4$
$\mathbb{F}$	-0.0209 ± 0.0015	0.5	-118.7 ± 50.7	4.15 ± 0.71	352.751	$356 - 3$
$\mathbb{F}$	-0.0221 ± 0.0016	0.7	-119.0 ± 51.3	4.39 ± 0.70	351.719	$356 - 3$
$\mathbb{F}$	-0.0236 ± 0.0018	1.0	-119.5 ± 52.1	4.68 ± 0.70	351.12	$356 - 3$
$v\mathbb{L}$	-0.0241 ± 0.0065	1.09	-119.7	4.75	371	$356 - 1$
$\mathbb{L}$	-0.0222 ± 0.0038	1.09	-119.7	4.75	345	$356 - 1$
$\mathbb{M}$	-0.0234 ± 0.002	1.09	-119.7	4.75	365	$356 - 1$
$\mathbb{H}$	-0.0246 ± 0.0054	1.09	-119.7	4.75	342	$356 - 1$

of the cross-correlation. We create 250 bootstrap samples by picking at random, with repetitions, 2370 $\xi_{\mathcal{P},A}$ cross-correlations from individual plates, and adding them accounting for their weights $W_{\mathcal{P},A}$. Then the CIV bias is fitted again for each of the bootstrap samples, and we obtain a final value and error for b_{Fc} from the mean and dispersion of these 250 bootstrap values. We find that this bootstrap error of the CIV bias matches the one obtained using the smoothed covariance matrix within 3 per cent.

5.4 Bias parameter with the smallest error

In previous papers on measuring the bias factor of absorbers, the combination $b_F(1 + \beta)$ has usually been used as one of the parameters to fit together with β, because of the small correlation of errors of these two quantities Slosar et al. (2011). Here, however, we can more precisely determine the combination that stays constant as we vary β_c, and has the smallest relative error marginalized over the other parameters. From Table 2, we find this combination to be (with a relative error that is the same as for the values listed in Table 2 when β_c is fixed),

$$b_{Fc}(1 + 0.44\beta_c) = -0.0170 \pm 0.0013. \tag{20}$$

This is a useful way to express our result, as the parameter we can measure with the highest accuracy.

6 ON THE TRANSMISSION BIAS

This paper has focused on deriving the transmission bias factor of the CIV absorption from the measurement of the cross-correlation of this absorption with quasars. However, a theoretical interpretation of this measurement requires a relation between this transmission bias factor and the large-scale bias factor of CIV absorbers. The bias of the absorbers is the ratio of the relative fluctuation in the density of absorbers to the relative mass fluctuation, and is equal to the large-scale bias factor of their host haloes.

We assume that this relation between the transmission and absorber bias factors is the general one derived in Font-Ribera & Miralda-Escudé (2012) for any class of absorption systems with absorption profiles that rarely overlap and that are correlated only with their host halo properties, but not with the surrounding large-scale structure (see their Section 4.3). We summarize here the derivation of this relation, starting with the definition of the transmission fluctuation of CIV absorbers δ_c, $F_c = \overline{F}_c(1 + \delta_c)$, where F_c is the flux transmission fraction due to CIV absorbers, and $\overline{F}_c$ is its average value. Defining the effective optical depth as $F_c = e^{-\tau_c}$ when averaged over a large-scale region, our assumption is that the effective

optical depth is the quantity that changes linearly with the density of absorbers in redshift space, and therefore the transmission fluctuation δ_c corresponds to an absorber density fluctuation $\delta_{\tau c}$ that is derived as:

$$
\begin{aligned}
\overline{F}_c(1 + \delta_c) &= e^{-\tau_c} = e^{-\overline{\tau}_c(1 + \delta_{\tau c})}, \\
&= \overline{F}_c(1 - \overline{\tau}_c \delta_{\tau c}); \\
\implies \delta_{\tau c} &= \frac{\delta_c}{\log \overline{F}_c}. \tag{21}
\end{aligned}
$$

The transmission and absorber bias factors and redshift distortion factors are therefore related as

$$b_{\tau c} = \frac{b_{Fc}}{\log \overline{F}_c}; \qquad \beta_{\tau c} = \beta_c. \tag{22}$$

This absorber bias factor should be equal to the bias factor of their host haloes. Note, however, that the host halo bias may not be just a function of the halo mass, if other properties such as assembly bias are important and correlate with the CIV cross-section.

In general, the redshift distortion factor should be given by the equation $\beta_c = b_{\tau \eta c} f(\Omega)/b_{\tau c}$, where $f(\Omega)$ is the logarithmic derivative of the growth factor, and $b_{\tau \eta c}$ is the peculiar velocity gradient bias of the absorbers. For this discussion, we assume that this peculiar velocity gradient bias is unity, and therefore $\beta_c = f(\Omega)/b_{\tau c}$, which is correct if the absorption profiles depend only on the host halo internal dynamics and are independent of the large-scale structure around them. This assumption is not true for the Lyα forest, where the absorption profiles are frequently overlapping and depend on the large-scale peculiar velocity gradient (see Arinyo-i-Prats et al. 2015).

Our measurement of β_c is therefore directly related to the absorber bias, but its measurement error is very large. To obtain a more reliable estimate of the absorber bias factor from our measurement of $b_{Fc}(1 + \beta_c)$, we need an independent estimate of $\overline{\tau}_c$.

6.1 The mean transmission of the CIV forest

For a population of uncorrelated absorbers, the mean transmission is related to the density of absorbers per unit redshift and equivalent width W_c, which we denote as $N(W_c, z)\, dW_c$. For the CIV doublet, the standard convention used in the literature is that the equivalent width W_c is that of the strongest line at $\lambda = 1548.2$ Å. The mean effective optical depth due to the CIV forest is then

$$
\begin{aligned}
\overline{\tau}_c(z) &= -\log(\overline{F}_c(z)) \\
&= \int_0^\infty dW_c \, \frac{N(W_c, z)\, W_c(1 + \bar{q}_c)(1 + z)}{\lambda_c}, \tag{23}
\end{aligned}
$$

where $\lambda_c = 1549.1$ Å is the mean rest-frame wavelength of the CIV doublet, and $\bar{q}_c$ is the average doublet equivalent width ratio of the absorbers (weighted by W_c).

To estimate $\bar{\tau}_c$, we use the observed equivalent width distributions obtained by D'Odorico et al. (2010) and Cooksey et al. (2013). The results of Cooksey et al. (2013) are more reliable at high equivalent width because they are based on a very large sample of quasars (SDSS DR7), whereas D'Odorico et al. (2010) use a smaller sample of quasar spectra with high resolution and signal to noise, allowing them to measure the distribution of weak absorption systems. We use an exponential distribution, which fits well the observations of Cooksey et al. (2013):

$$N(W_c, z) = k \exp(-W_c/W_*). \tag{24}$$

We take the fitted values for k and W_* from table 4 of Cooksey et al. (2013), for their redshift range $2.24 \le z < 2.51$, which best corresponds to our middle redshift range $\mathbb{M}$ ($2.15 \le z < 2.6$) containing most of our absorption systems. The values are $W_* = 0.368$ Å, and $kW_* = 4.84$ (we have converted the value of k reported by Cooksey et al. 2013) to a density of systems per unit redshift, which is the directly observed quantity, instead of density per unit X, where $dX = dz(1 + z)^2 H_0/H(z)$, a quantity often used in studies of absorption systems). The distribution of CIV equivalent widths has been found to evolve only weakly over the redshift range covered by the SDSS data. We ignore any possible redshift evolution and we use our results for the full sample (see their table 4).

Integrating equation (23) with the exponential form of the equivalent width distribution, we find

$$\bar{\tau}_c = \frac{(1 + \bar{q})(1 + z)kW_*^2}{\lambda_c}. \tag{25}$$

We use a mean doublet ratio $\bar{q} = 0.695 \pm 0.010$ from the mean value measured in Mas-Ribas et al. (2017) for CIV systems associated with DLAs, noting that the mean equivalent width of the CIV line in DLAs found in Mas-Ribas et al. (2017) is $\bar{W}_c = 0.429$ Å, only slightly larger than W_*, implying a similar degree of line saturation and therefore of the value of $\bar{q}$. At a mean redshift $z = 2.37$, this yields a value $\bar{\tau}_c = 0.00657$.

We now correct this value for the fact that the true equivalent width distribution does not follow the exponential form at $W_c < 0.5$ Å, where the SDSS data used in Cooksey et al. (2013) starts being incomplete. Instead, the CIV equivalent width distribution can be fitted by the power-law $N(W_c, z) \propto W_c^{-\alpha}$ at low equivalent widths, where $\alpha = 1.53$ fits well the results of D'Odorico et al. (2010) down to the lowest equivalent widths at which they are complete (see their figure 2). We assume we can treat the systems as optically thin for the low column densities at which we use their model, so that CIV column densities are proportional to equivalent widths. We match the power-law and equivalent width distributions at $W_c = 1.4W_* = 0.515$ Å, which is roughly where the results of D'Odorico et al. (2010) and Cooksey et al. (2013) match (see figure 10 in Cooksey et al. 2013), and also the equivalent width below which the data of Cooksey et al. (2013) start being incomplete. Assuming a fixed value $1 + \bar{q} = 1.695$, we replace the function N by

$$N_{corr} = k \exp(-W_c/W_*), \quad (W_c > 1.4W_*); \tag{26}$$

$$N_{corr} = k \exp(-1.4) \left(\frac{W_c}{1.4W_*}\right)^{-1.53}, \quad (W_c < 1.4W_*). \tag{27}$$

The corrected value with this distribution is found to be $\bar{\tau}_c = 0.0106$. Finally, we note that the correction to this effective optical depth arising from the difference between the exponential distribution and

the power-law distribution at $W_c < 1.4W_*$, which is $\Delta\bar{\tau}_c = 0.0040$, probably has an average value of $1 + \bar{q}$ that is intermediate between the value $1 + \bar{q} = 1.695$ for DLAs found by Mas-Ribas et al. (2017), and the limiting value for optically thin absorbers, $1 + \bar{q} = 1.5$. Adopting an intermediate value $1 + \bar{q} = 1.6$ for this correction to the W_c distribution, we reduce the correction to $\Delta\bar{\tau}_c = 0.0040 \times (1.6/1.695)$, and we obtain our final estimate $\bar{\tau}_c = 0.0103$.

The error on our estimate of $\bar{\tau}_c$ is dominated by the uncertainties in the W_c distribution and its redshift evolution, in particular by the slope of the power-law distribution and how far down it extends to low W_c. An error ± 0.1 to the power-law slope in α implies an error of ~ 10 per cent in $\bar{\tau}_c$. We note also that the low-W_c absorbers tend to be clustered with the high W_c ones because they often result from de-blending of complex absorption profiles, which may have led us to an overestimate of $\bar{\tau}_c$, but this is difficult to estimate. We therefore urge the total absorption by all detected absorbers to be directly reported in future studies of weak metal-line systems.

An alternative method to measure the mean CIV optical depth is by directly using the pixel distribution of the ratios of CIV to HI optical depths. The results obtained with this method by Schaye et al. (2003) show a power-law relation of the CIV and HI optical depths with the approximate form $\tau_c \propto \tau_{HI}^{0.8}$, down to the lowest detectable values (see their figure 4). This suggests that the power-law equivalent width distribution of D'Odorico et al. (2010), with index -1.53 [equation (27)], translates to a power-law equivalent width distribution for Ly α forest absorbers with index $-1.53 \times 0.8 + 0.2 = 1.42$ similar to what is observed at low column densities for the Ly α forest. A large contribution to the total CIV optical depth from very weak CIV absorbers would require either a steepening of the HI column density distribution at low N_{HI}, or a flattening of the relation of τ_c to τ_{HI}, which the observations do not indicate.

7 DISCUSSION

7.1 The bias of the CIV absorbers

Having estimated $\bar{\tau}_c$, we can now infer the average bias of the CIV absorbers. We use our result for the parameter with the smallest relative error from equation (20):

$$(1 + 0.44\beta_c)b_{Fc} \simeq -0.0170 \pm 0.0013. \tag{28}$$

Using $\beta_c = f(\Omega)/b_{\tau c}$, $b_{Fc} = -\bar{\tau}_c b_{\tau c}$, and a value $f(\Omega) \simeq 0.97$ for the cosmological model we use at the mean redshift of our sample, we obtain

$$(0.44 + 1/\beta_c)\bar{\tau}_c = 0.0175 \pm 0.0014. \tag{29}$$

If the mean optical depth is in the range $0.008 < \bar{\tau}_c < 0.012$ (a generously broad range given our previous discussion on uncertainties in the determination of this quantity), the previous equality implies $0.6 < \beta_c < 1.0$. This is consistent with our measurement of β_c from the anisotropy of the quasar-CIV cross-correlation, and with a bias factor of the CIV absorbers that is roughly in the range $1 < b_{\tau c} < 1.7$. This bias factor is less than that of DLAs, for which $b_{DLA} \simeq 2$ Pérez-Ràfols et al. (2018), indicating that the general population of CIV absorbers tends to be in less massive haloes than DLAs.

This conclusion needs to be taken as preliminary until the value of $\bar{\tau}_c$ and the CIV transmission bias factor are measured more reliably, with a better control on the systematic errors.

7.2 Relation to the host halo bias factor

The bias of metal lines can be modelled theoretically assuming that the gas causing metal absorption is associated with host haloes with a certain mass distribution. Metals are created in haloes if the massive stars in which they are synthesized are all formed in the virialized regions of haloes. Galactic winds can then eject the metal-enriched gas outside the virialized regions, into the low-density intergalactic gas surrounding haloes. The photoionized intergalactic medium contains substantial CIV down to densities as low as the mean density of the universe (see e.g. figure 3 in Schaye et al. 2003), so many CIV absorbers may arise far from the virialized regions of haloes. This, however, does not alter the equality of the bias factor of the CIV absorbers to the bias factor of the haloes they originated from, on scales larger than the size of the galactic winds, or the largest distance that the metal-enriched wind can traverse.

Any large-scale structure model predicts a number density of haloes $n(M)\,\mathrm{d}M$ of mass M in a bin $\mathrm{d}M$. If a line of sight intercepts a halo, a metal line can be observed with some equivalent width W_c. A useful concept to define is the *absorption volume* of the metal line produced by a halo, equal to

$$V_c(M) = \int \mathrm{d}^2 x \, \frac{W_c(1 + \bar{q}_c)(1 + z)}{\lambda_c} \, \frac{c}{H(z)}, \tag{30}$$

where the integral is done over the projected area of the halo seen from a specific line of sight, with comoving coordinates x in the perpendicular directions. The volume V_c is then obtained in comoving units, and is defined to be an average over all haloes of mass M. The mean absorption of CIV systems is then given by

$$\bar{\tau}_c = \int \mathrm{d}M \, n(M) \, V_c(M). \tag{31}$$

Large-scale structure models predict the bias $b_h(M)$ of haloes of mass M, and the bias factors of CIV systems are related to this by

$$b_{Fc} = -\int \mathrm{d}M n(M) \, b_h(M) \, V_c(M);$$

$$b_{\tau c} = -\frac{b_{Fc}}{\bar{\tau}_c} = \frac{1}{\bar{\tau}_c} \int \mathrm{d}M n(M) \, b_h(M) \, V_c(M). \tag{32}$$

This relation assumes that the CIV absorption volume V_c does not depend on any halo property that can alter the value of the bias factor, except for the halo mass. In particular, the presence of assembly bias [the dependence of halo bias on its formation time at a fixed mass; see Borzyszkowski et al. (2017)] alters this relation if V_c depends also on the halo formation time.

We point out the distinction between the average bias factors of CIV absorbers, for which every absorber is weighted equally and the host haloes are weighted by their mean cross-section to produce an absorber, and the average bias factor of the CIV transmission fluctuation, which we have measured here and should be compared to the host halo bias weighted by the absorption volume we have defined here. The absorption volume should increase with halo mass faster than the cross-section (because of the increase of velocity dispersion with halo mass), and therefore the absorption-volume weighted bias factor should be higher than the cross-section weighted one. This further supports the conclusion that the CIV absorbers contributing to the mean CIV transmission are hosted by haloes of lower bias (i.e. less massive haloes) than DLAs.

7.3 Comparison to other work

Vikas et al. (2013) also measured the cross-correlation of CIV absorbers with quasars, but using individually identified CIV systems.

They translated an isotropic measurement of the cross-correlation to a CIV bias factor of $b_c = 2.38 \pm 0.62$. The bias inferred for their individual CIV absorbers should be the same as our absorber bias $b_{\tau c}$, under the assumption that the weak systems that are not detected in the catalogue used by Vikas et al. (2013) have the same bias factor as the mean of all the CIV systems weighted by their equivalent width, which determines our CIV transmission bias factor. As mentioned previously, the principal uncertainty in comparing the two results is the value of $\bar{\tau}_c$. In addition, our analysis has included the redshift space distortion factor β_c, whereas Vikas et al. (2013) did only an isotropic analysis. The two measurements are not inconsistent taking into account the large errors in both of them, however they suggest that weak CIV systems may have lower bias than strong ones, which would help explain why the individually detected CIV systems have a higher bias than the overall population.

Next, we comment on the result of Blomqvist et al. (2018), who have simultaneously completed a similar analysis to ours including eBOSS data. Apart from having a larger data set (especially at low redshift), there are other differences in the two analyses. One is the different continuum-fitting methods. Blomqvist et al. (2018) apply the same continuum-fitting method used in other BOSS analyses of the Lyα forest, hence the need for a distortion matrix in their work (i.e. their Section 5.2). They also use an upgrade from the Baofit code we use called *picca* ,[4] although this should not affect the results. Their fitting range extends to a larger scale than ours: from 10 to 180 h^{-1} Mpc, compared to our range from 5 to 60 h^{-1} Mpc.

We focus on comparing their result for the bias and redshift distortion factors when restricting the rest-frame wavelength range to $1420\,\text{Å} \leq \lambda_{\mathrm{RF}} < 1520\,\text{Å}$, the same one we have used which avoids the contribution from SiIV lines. The mean result of Blomqvist et al. (2018) for their entire redshift range is $\beta_c = 0.35 \pm 0.21$, and $b_c(1 + \beta_c) = -0.019 \pm 0.002$. In comparison, we obtain a higher value of the redshift distortion factor, $\beta_c = 1.09 \pm 0.56$, although the large errors do not make the two values incompatible. Our value for the bias b_c agrees with theirs: from our equation (20), if we use their central value $\beta_c = 0.35$, we find that our measurement $b_c(1 + 0.44\beta_c) = -0.017$ implies $b_c(1 + \beta_c) = -0.0199 \pm 0.0015$ for $\beta_c = 0.35$, in full agreement with Blomqvist et al. (2018).

The low central value of β_c found by Blomqvist et al. (2018) is not consistent with our constraint derived from the bounds in $\bar{\tau}_c$ from measurements of the incidence rate of CIV absorbers as a function of their equivalent width in Section 7.1, implying $0.6 < \beta_c < 1$. Taking into account the measurement error, however, their result can be compatible with this constraint. It is worth noting that their result for β_c is substantially different when dividing the data set into two redshift intervals. For low redshift ($z < 2.2$ and a mean effective redshift $z_{\mathrm{eff}} = 1.69$), they find $\beta_c = 0.05 \pm 0.19$, whereas for high redshift ($z > 2.2$ and $z_{\mathrm{eff}} = 2.41$, closer to our measurement with $z_{\mathrm{eff}} = 2.29$) their result is $\beta_c = 0.67 \pm 0.29$. Their result at high redshift is therefore fully consistent with ours, and with our derived constraint from the value of $\bar{\tau}_c$. The very low value of β_c at low redshift derived by Blomqvist et al. (2018) suggests that the absorber bias factor $b_{\tau c}$ may be increasing rapidly with decreasing redshift, perhaps because CIV is being destroyed in low-mass haloes and being formed in massive haloes. However, more data at low redshift that allow reduced error bars and testing of systematics is necessary before one can draw solid conclusions on the redshift evolution of the bias and redshift distortion factors.

---

[4] https://github.com/igmhub/picca/

8 CONCLUSIONS

With the final SDSS-III Data Release, we have measured the cross-correlation of the CIV forest absorption with quasars. We found that the simple linear theory model for this cross-correlation, with the redshift distortions as predicted by Kaiser (1987), is fully consistent with the data, and we have obtained the CIV transmission bias factor required to match the measured cross-correlation amplitude. Our main results are

(i) We measure $(1 + \beta_c)b_{Fc} = -0.024 \pm 0.003$, and $\beta_c = 1.1 \pm 0.6$ at redshift $z = 2.3$, from a fit obtained over a radial range $5\,h^{-1}$ Mpc $< r < 60\,h^{-1}$ Mpc. The value of β_c is highly uncertain, but we can determine most accurately the combination $(1 + 0.44\beta_c)b_{Fc} = -0.0170 \pm 0.0013$.

(ii) The CIV transmission bias does not show any detectable redshift evolution over the range $1.72 < z < 2.85$.

(iii) Using a derived value of $\bar{\tau}_c(z) \simeq 0.01$ from measurements of the equivalent width distribution of CIV absorbers in the literature, with a generous uncertainty of $20\,\mathrm{per\,cent}$, we infer a redshift distortion parameter in the range $0.6 < \beta_c < 1$, and an absorber bias factor in the range $1 < b_{\tau c} < 1.7$, which is substantially lower than the bias factor of DLAs. This suggests that the CIV absorption systems dominating the total CIV mean absorption are hosted in haloes of lower mass than DLAs, at our mean redshift $z \sim 2.3$. The measurements of β_c by Blomqvist et al. (2018) also suggest this may be changing at lower redshifts, $z \sim 1.7$, with more CIV systems being present in more massive haloes. Better measurements of $\bar{\tau}_c$ and β_c at different redshifts are required to test the validity of these preliminary conclusions.

REFERENCES

Ade P. A. R. et al., 2016, A&A, 594, A13
Alam S. et al., 2015, ApJS, 219, 12
Arinyo-i-Prats A., Miralda-Escudé J., Viel M., Cen R., 2015, JCAP, 12, 017
Bahcall J. N., Spitzer L., Jr., 1969, ApJ, 156, L63
Bautista J. E. et al., 2017, A&A, 603, A12
Bird S., Rubin K. H. R., Suresh J., Hernquist L., 2016, MNRAS, 462, 307
Blomqvist M. et al., 2015, JCAP, 11, 034
Blomqvist M. et al., 2018, JCAP, 5, 029
Boksenberg A., Sargent W. L. W., 2015, ApJS, 218, 7
Bolton A. S. et al., 2012, AJ, 144, 144
Borzyszkowski M., Porciani C., Romano-Díaz E., Garaldi E., 2017, MNRAS, 469, 594
Bovy J. et al., 2011, ApJ, 729, 141
Busca N. G. et al., 2013, A&A, 552, A96
Coil A. L. et al., 2008, ApJ, 672, 153
Cole S., Kaiser N., 1989, MNRAS, 237, 1127
Cooksey K. L., Kao M. M., Simcoe R. A., O'Meara J. M., Prochaska J. X., 2013, ApJ, 763, 37
Croft R. A. C., Weinberg D. H., Katz N., Hernquist L., 1998, ApJ, 495, 44
Croft R. A. C., Weinberg D. H., Pettini M., Hernquist L., 1999, ApJ, 520, 1
Croft R. A. C., Weinberg D. H., Bolte M., Burles S., Hernquist L., Katz N., Kirkman D., Tytler D., 2002, ApJ, 581, 20
Croom S. M. et al., 2005, MNRAS, 356, 415
D'Odorico V., Calura F., Cristiani S., Viel M., 2010, MNRAS, 401, 2715
D'Odorico V. et al., 2016, MNRAS, 463, 2690
Dawson K. S. et al., 2013, AJ, 145, 10
Delubac T. et al., 2015, A&A, 574, A59
du Mas des Bourboux H. et al., 2017, A&A, 608, A130
Eftekharzadeh S. et al., 2015, MNRAS, 453, 2779
Eisenstein D. J. et al., 2011, AJ, 142, 72
Font-Ribera A., Miralda-Escudé J., 2012, JCAP, 7, 028
Font-Ribera A. et al., 2012, JCAP, 11, 059
Font-Ribera A. et al., 2013, JCAP, 5, 018
Font-Ribera A. et al., 2014, JCAP, 5, 027
Fukugita M., Ichikawa T., Gunn J. E., Doi M., Shimasaku K., Schneider D. P., 1996, AJ, 111, 1748
Gunn J. E. et al., 1998, AJ, 116, 3040
Gunn J. E. et al., 2006, AJ, 131, 2332
Hopkins A. M., Beacom J. F., 2006, ApJ, 651, 142
Kaiser N., 1987, MNRAS, 227, 1
Kirkby D. et al., 2013, JCAP, 1303, 024
Kirkpatrick J. A., Schlegel D. J., Ross N. P., Myers A. D., Hennawi J. F., Sheldon E. S., Schneider D. P., Weaver B. A., 2011, ApJ, 743, 125
Laurent P. et al., 2016, JCAP, 1611, 060
Laurent P. et al., 2017, JCAP, 1707, 017
Lundgren B. et al., 2013, in American Astronomical Society Meeting Abstracts #221. p. 402.05
Lynds R., 1971, ApJ, 164, L73
Mas-Ribas L. et al., 2017, ApJ, 846, 4
McDonald P., Miralda-Escudé J., Rauch M., Sargent W. L. W., Barlow T. A., Cen R., Ostriker J. P., 2000, ApJ, 543, 1
McDonald P. et al., 2006, ApJS, 163, 80
Miralda-Escudé J., Cen R., Ostriker J. P., Rauch M., 1996, ApJ, 471, 582
Myers A. D., Brunner R. J., Nichol R. C., Richards G. T., Schneider D. P., Bahcall N. A., 2007a, ApJ, 658, 85
Myers A. D., Brunner R. J., Richards G. T., Nichol R. C., Schneider D. P., Bahcall N. A., 2007b, ApJ, 658, 99
Pâris I. et al., 2012, A&A, 548, A66
Pâris I. et al., 2014, A&A, 563, A54
Pâris I. et al., 2017, A&A, 597, A79
Pérez-Ràfols I. et al., 2018, MNRAS, 473, 3019

Pieri M. M., 2014, MNRAS, 445, L104

Rauch M., 1998, ARA&A, 36, 267

Rauch M., Haehnelt M. G., Steinmetz M., 1997, ApJ, 481, 601

Richards G. T. et al., 2009, ApJS, 180, 67

Ross N. P. et al., 2009, ApJ, 697, 1634

Ross N. P. et al., 2012, ApJS, 199, 3

Sargent W. L. W., Young P. J., Boksenberg A., Tytler D., 1980, ApJS, 42, 41

Schaye J., Aguirre A., Kim T.-S., Theuns T., Rauch M., Sargent W. L. W., 2003, ApJ, 596, 768

Shen Y. et al., 2007, Astron. J., 133, 2222

Shen Y. et al., 2009, ApJ, 697, 1656

Slosar A. et al., 2011, JCAP, 9, 001

Slosar A. et al., 2013, JCAP, 4, 026

Tinker J. L., Robertson B. E., Kravtsov A. V., Klypin A., Warren M. S., Yepes G., Gottlober S., 2010, ApJ, 724, 878

Vikas S. et al., 2013, ApJ, 768, 38

Weymann R. J., Morris S. L., Foltz C. B., Hewett P. C., 1991, ApJ, 373, 23

White M. et al., 2012, MNRAS, 424, 933

Yèche C. et al., 2010, A&A, 523, A14

York D. G. et al., 2000, AJ, 120, 1579

This paper has been typeset from a TEX/LATEX file prepared by the author.